Multibaric–Multithermal Molecular Dynamics Simulation of Alanine Dipeptide in Explicit Water

Hisashi Okumura* **and Yuko Okamoto**

Department of Physics, School of Science, Nagoya University, Furo-cho, Chikusa-ku, Nagoya 464-8602

Received November 13, 2006; E-mail: hokumura@tb.phys.nagoya-u.ac.jp

Multibaric–multithermal (MUBATH) simulation can escape from local-minimum free-energy states, and one can obtain accurate thermodynamic quantities as functions of any temperature and pressure from a single simulation run. We performed a MUBATH molecular dynamics simulation of an alanine dipeptide in explicit water. The MUBATH simulation sampled the states of P_{II}, C_5, α_R, α_P, and α_L. On the other hand, the conventional isobaric–isothermal simulation was trapped in local-minimum free-energy states and sampled only a few of them. We calculated the partial molar enthalpy and partial molar volume from the MUBATH simulation. Our results were in accord with those from Raman spectroscopy.

Peptides and proteins have complicated free-energy surfaces with many local minima. Conventional molecular dynamics (MD) and Monte Carlo (MC) simulations in the canonical[1–4] or isobaric–isothermal[5,6] ensemble tend to get trapped in these local-minimum states and can sample only a limited range of configurational space (giving inaccurate results). In order to avoid this difficulty, generalized-ensemble simulations are commonly performed.[7–9] One of the most well-known generalized-ensemble algorithms is the multicanonical algorithm.[10–13] In the multicanonical ensemble, a non-Boltzmann weight factor is used so that a free one-dimensional random walk in the potential-energy space can be realized. Thus, a simulation with this algorithm does not get trapped in free-energy-minimum states and is able to sample a wide range of the configurational space. It is also possible to obtain various canonical-ensemble averages in a wide range of temperature from a single simulation run by the reweighting techniques.[14] However, the simulation is performed in a fixed volume, and the pressure cannot be specified as in experimental environment.

In order to overcome this difficulty, we have recently proposed multibaric–multithermal (MUBATH) MC[15–17] and MD[18,19] methods. This is an extension of the multicanonical simulation, which can perform two-dimensional random walks not only in the potential-energy space but also in the volume space. The MUBATH algorithm has the following advantages; (1) It allows the simulation to escape from local-minimum-energy states and to sample the configurational space more widely than the conventional isobaric–isothermal method. (2) One can obtain various isobaric–isothermal ensembles not only at any temperature as in the multicanonical algorithm, but also at any pressure from only one simulation run. (3) One can control temperature and pressure so that we can compare the simulation results with those by experiments under the same conditions.

The MUBATH algorithm has been utilized to calculate the equation of states for a super critical fluid[15,16,18,19] and to investigate the liquid–gas phase transition of a Lennard–Jones fluid.[17] In this article, we report the results of our applications of the MUBATH MD method to an alanine dipeptide in explicit water. This is the first work to apply the MUBATH MD algorithm to a biomolecular system. The alanine dipeptide has been studied theoretically extensively as a model biomolecule because of its simplicity.[20–25] Experimentally, Takekiyo et al. have recently performed Raman spectroscopy experiments under several temperatures and pressures.[26] They discussed partial molar enthalpy difference and partial molar volume difference among some states of alanine dipeptide. There is no simulational study that is related to these experiments. In this article, the efficiency of the MUBATH algorithm is discussed along with a comparison of the physical properties of the alanine dipeptide obtained from the MUBATH MD simulation with those from Raman spectroscopy at several temperatures and pressures.

In the next section, the algorithm of the MUBATH MD method is explained. Computational details of our MD simulations are described in the third section. Results and discussion are presented in the fourth section. The last section is devoted to conclusions.

Methods

In the isobaric–isothermal ensemble,[5,6] the distribution $\mathcal{P}_{NPT}(E,V)$ of potential energy E and volume V is given by

$$\mathcal{P}_{NPT}(E,V) = n(E,V)\mathrm{e}^{-\beta_0 H}, \tag{1}$$

where $n(E,V)$ is the density of states as a function of E and V, β_0 is the inverse of the product of the Boltzmann constant k_B and absolute temperature T_0, at which simulations are performed, and H is the "enthalpy" (without the kinetic energy contributions): $H = E + P_0 V$. Here, P_0 is the pressure at which simulations are performed. This ensemble has bell-shaped distributions both in the potential-energy space and in the volume space.

In the MUBATH ensemble,[15–19] every state is sampled with a weight factor $W_{\mathrm{mbt}}(E,V) \equiv \exp\{-\beta_0 H_{\mathrm{mbt}}(E,V)\}$ so that a uniform distribution of both E and V may be obtained:

$$\mathcal{P}_{\mathrm{mbt}}(E,V) = n(E,V)W_{\mathrm{mbt}}(E,V) = \text{constant}. \tag{2}$$

Published on the web June 13, 2007; doi:10.1246/bcsj.80.1114

Here, $W_{\rm mbt}(E, V)$ and $H_{\rm mbt}$ are referred to as the MUBATH weight factor and the MUBATH enthalpy, respectively. The difference between $H_{\rm mbt}$ and H is written as $\delta H(E, V)$: $H_{\rm mbt}(E, V) = H + \delta H(E, V)$. The difference $\delta H(E, V)$ is therefore characteristic of the MUBATH simulation ($\delta H(E, V) = 0$ gives the regular isobaric–isothermal simulation).

In the preceding articles,[18,19] we have described the MUBATH MD algorithm for a system consisting of spherical atoms. In this article, we explain the MUBATH algorithm for a system consisting of both spherical atoms and rigid-body molecules. The number of atoms in the flexible peptide molecule is N and that of the rigid-body water molecules is M. Atoms in the flexible model molecule are treated in the same way as monatomic molecules in the MD simulations. The Hamiltonian $\mathcal{H}_{\rm mbt}$ for the present system is given by the combination of the MUBATH Hamiltonian[18,19] with the Hamiltonian for rigid-body molecules in the isobaric–isothermal ensemble.[27] The isobaric–isothermal Hamiltonian is based on the Nosé thermostat[1,2] and the Andersen barostat[5] with the rigid-body-molecule Hamiltonian:[28]

$$\begin{aligned}\mathcal{H}_{\rm mbt} = {} & \sum_{i=1}^{N+M} \frac{\tilde{\boldsymbol{p}}_i^2}{2m_i V^{\frac{2}{3}} s^2} + \sum_{j=1}^{M} \frac{1}{8s^2} \tilde{\boldsymbol{\pi}}_j^{\rm T} \boldsymbol{S}(\boldsymbol{q}_j) \boldsymbol{D}_j \boldsymbol{S}^{\rm T}(\boldsymbol{q}_j) \tilde{\boldsymbol{\pi}}_j \\ & + E(V^{\frac{1}{3}}\tilde{\boldsymbol{r}}, \boldsymbol{q}) + \frac{P_V^2}{2W} + P_0 V + \frac{P_s^2}{2Q} \\ & + g k_{\rm B} T_0 \log s + \delta H(E(V^{\frac{1}{3}}\tilde{\boldsymbol{r}}, \boldsymbol{q}), V), \end{aligned} \tag{3}$$

where the superscript T in $\tilde{\boldsymbol{\pi}}_j^{\rm T}$ stands for transpose, the summation with respect to i is taken over both N atoms and M rigid-body molecules and that with respect to j over only M rigid-body molecules. The variable $\tilde{\boldsymbol{r}}_i$ is the coordinates scaled by the length of the simulation box: $\tilde{\boldsymbol{r}}_i = V^{-\frac{1}{3}}\boldsymbol{r}_i$ ($\boldsymbol{r}_i$ is the real coordinate). We have introduced a simplified notation for the set of the scaled coordinates: $\tilde{\boldsymbol{r}} \equiv \{\tilde{\boldsymbol{r}}_1, \tilde{\boldsymbol{r}}_2, \ldots, \tilde{\boldsymbol{r}}_{N+M}\}$. When i indicates a rigid-body molecule, $\boldsymbol{r}_i$ stands for the coordinate of its center of mass. The variable $\tilde{\boldsymbol{p}}_i$ is the conjugate momentum for $\tilde{\boldsymbol{r}}_i$. The real momentum $\boldsymbol{p}_i$ is related to the virtual momentum $\tilde{\boldsymbol{p}}_i$ by $\boldsymbol{p}_i = \tilde{\boldsymbol{p}}_i / V^{\frac{1}{3}} s$, where s is the additional degree of freedom for the Nosé thermostat. The variables P_V and P_s are the conjugate momenta for V and s, respectively. The constant m_i is the mass of atom i or rigid-body molecule i. The constants W and Q are the artificial "mass" related to V and s, respectively. The real time interval Δt is associated with the virtual time interval $\Delta\tilde{t}$ by the relation $\Delta t = \Delta\tilde{t}/s$. In the case of the system consisting of N atoms and M rigid-body molecules, g equals $3N + 6M$ if the time development is performed in the real time t, or g equals $3N + 6M + 1$ if the time development is performed in the virtual time $\tilde{t}$. The variable $\boldsymbol{q}$ is a quaternion which specifies the orientation of the rigid-body molecule. Here, the quaternion $\boldsymbol{q} = (q_0, q_1, q_2, q_3)$ is related to the Euler angle (ϕ, θ, ψ) as follows:

$$q_0 = \cos\left(\frac{\theta}{2}\right)\cos\left(\frac{\phi + \psi}{2}\right), \tag{4}$$

$$q_1 = \sin\left(\frac{\theta}{2}\right)\cos\left(\frac{\phi - \psi}{2}\right), \tag{5}$$

$$q_2 = \sin\left(\frac{\theta}{2}\right)\sin\left(\frac{\phi - \psi}{2}\right), \tag{6}$$

$$q_3 = \cos\left(\frac{\theta}{2}\right)\sin\left(\frac{\phi + \psi}{2}\right). \tag{7}$$

The element of the matrix $\boldsymbol{S}(\boldsymbol{q})$ is given by

$$\boldsymbol{S}(\boldsymbol{q}) = \begin{pmatrix} q_0 & -q_1 & -q_2 & -q_3 \\ q_1 & q_0 & -q_3 & q_2 \\ q_2 & q_3 & q_0 & -q_1 \\ q_3 & -q_2 & q_1 & q_0 \end{pmatrix}. \tag{8}$$

The variable $\tilde{\boldsymbol{\pi}}_j$ is the conjugate momentum for $\boldsymbol{q}_j$. The real momentum of the quaternion $\boldsymbol{\pi}_j$ is related to $\tilde{\boldsymbol{\pi}}_j$ by $\boldsymbol{\pi}_j = \tilde{\boldsymbol{\pi}}_j / s$. The matrix $\boldsymbol{D}$ is a 4×4 matrix consisting of the inverse of the principal moments of inertia I_1, I_2, and I_3:

$$\boldsymbol{D} = \begin{pmatrix} 0 & 0 & 0 & 0 \\ 0 & I_1^{-1} & 0 & 0 \\ 0 & 0 & I_2^{-1} & 0 \\ 0 & 0 & 0 & I_3^{-1} \end{pmatrix}. \tag{9}$$

The equations of motion are obtained from the Hamiltonian in Eq. 3. In order to write the equations of motion more elegantly, we may introduce the angular velocity

$$\boldsymbol{\omega} = (\omega_1, \omega_2, \omega_3)^{\rm T} \tag{10}$$

and the four-dimensional angular velocity

$$\boldsymbol{\omega}^{(4)} = (0, \omega_1, \omega_2, \omega_3)^{\rm T}, \tag{11}$$

where ω_1, ω_2, and ω_3 are the angular velocity along each of the corresponding principal axes. Here, $\boldsymbol{\omega}$ and $\boldsymbol{\omega}^{(4)}$ are treated as a 3×1 matrix and a 4×1 matrix, respectively.

$$\boldsymbol{\omega}_j^{(4)} = \frac{1}{2}\boldsymbol{D}_j \boldsymbol{S}^{\rm T}(\boldsymbol{q}_j)\boldsymbol{\pi}_j. \tag{12}$$

The equations of motion in the real time development are then given by

$$\dot{\boldsymbol{r}}_i = \frac{\boldsymbol{p}_i}{m_i} + \frac{\dot{V}}{3V}\boldsymbol{r}_i, \tag{13}$$

$$\dot{\boldsymbol{p}}_i = \left(1 + \frac{\partial \delta H}{\partial E}\right)\boldsymbol{F}_i - \left(\frac{\dot{V}}{3V} + \frac{\dot{s}}{s}\right)\boldsymbol{p}_i, \tag{14}$$

$$\dot{\boldsymbol{q}}_j = \frac{1}{2}\boldsymbol{S}(\boldsymbol{q}_j)\boldsymbol{\omega}_j^{(4)}, \tag{15}$$

$$\boldsymbol{I}_j \dot{\boldsymbol{\omega}}_j = \left(1 + \frac{\partial \delta H}{\partial E}\right)\boldsymbol{N}_j - \boldsymbol{\omega}_j \times (\boldsymbol{I}_j \boldsymbol{\omega}_j) - \frac{\dot{s}}{s}\boldsymbol{I}_j \boldsymbol{\omega}_j, \tag{16}$$

$$\dot{V} = s\frac{P_V}{W}, \tag{17}$$

$$\begin{aligned}\dot{P}_V = s\Bigg[& \frac{1}{3V}\left\{\sum_{i=1}^{N+M}\frac{\boldsymbol{p}_i^2}{m_i} + \left(1 + \frac{\partial \delta H}{\partial E}\right)\sum_{i=1}^{N+M}\boldsymbol{F}_i \cdot \boldsymbol{r}_i\right\} \\ & - \left(P_0 + \frac{\partial \delta H}{\partial V}\right)\Bigg], \end{aligned} \tag{18}$$

$$\dot{s} = s\frac{P_s}{Q}, \tag{19}$$

$$\dot{P}_s = \sum_{i=1}^{N+M}\frac{\boldsymbol{p}_i^2}{m_i} + \sum_{j=1}^{M}\boldsymbol{\omega}_j^{\rm T}\boldsymbol{I}_j\boldsymbol{\omega}_j - g k_{\rm B} T_0, \tag{20}$$

where $\boldsymbol{I}$ is the 3×3 diagonal matrix, of which the diagonal elements are the principal moments of inertia I_1, I_2, and I_3. The vector $\boldsymbol{F}_i$ stands for the force acting on atom i if i indicates an atom in the flexible molecule or the total force on all the atoms in molecule i if i indicates a rigid-body molecule. The vector $\boldsymbol{N}_j$ is the torque on rigid molecule j. Performing the MD simulation by the equations of motion in Eqs. 13–20, the MUBATH distribution $\mathcal{P}_{\rm mbt}(E, V)$ in Eq. 2 is obtained.

For the actual time development in Eqs. 13–20, a symplectic integrator[29] was employed in the present simulations. We used the symplectic time-development formalism,[27] which is based on the Nosé–Poincaré thermostat,[30,31] the Andersen barostat,[5] and the symplectic quaternion scheme.[28] The Nosé–Poincaré thermostat gives the same equations of motion as the Nosé thermostat and provides a symplectic integrator. Combining these three algorithms, we performed the time development by the symplectic integrator throughout the simulation. The symplectic integrator has the advantage that the secular deviation of the value of the Hamiltonian is suppressed.

In the case of $\delta H(E, V) = 0$, the Hamiltonian in Eq. 3 and the equations of motion in Eqs. 13–20 become those for the regular isobaric–isothermal MD simulation of the Nosé–Andersen formulation for the system consisting of both flexible and rigid-body molecules. The MUBATH weight factor is, however, not a priori known and has to be determined, for example, by the usual iterations of short simulations.[32–34]

After an optimal weight factor $W_{\rm mbt}(E, V)$ is determined, a long production run is performed for data collection. We used the reweighting techniques[14] for the results of the production run to calculate the isobaric–isothermal-ensemble averages. The probability distribution $\mathcal{P}_{NPT}(E, V; T, P)$ in the isobaric–isothermal ensemble at the desired temperature T and pressure P is given by

$$\mathcal{P}_{NPT}(E, V; T, P) = \frac{\mathcal{P}_{\rm mbt}(E, V)\ W^{-1}_{\rm mbt}(E, V)\ {\rm e}^{-\beta(E+PV)}}{\displaystyle\int {\rm d}V \int {\rm d}E\ \mathcal{P}_{\rm mbt}(E, V)\ W^{-1}_{\rm mbt}(E, V)\ {\rm e}^{-\beta(E+PV)}}. \tag{21}$$

The expectation value of a physical quantity A at T and P is then obtained from

$$\langle A \rangle_{NPT} = \int {\rm d}V \int {\rm d}E\ A(E, V)\ \mathcal{P}_{NPT}(E, V; T, P). \tag{22}$$

Because of the random walks both in the potential-energy space and in the volume space, we can calculate physical quantities in wide ranges of T and P.

Computational Details

The MUBATH MD simulation was performed for a system consisting of one alanine dipeptide molecule ((*S*)-2-(acetylamino)-*N*-methylpropanamide) and 63 water molecules. This peptide molecule is not a dipeptide in a strict sense, which consists of two amino acids, but has been conventionally called an alanine dipeptide. We used enough water molecules so that the alanine dipeptide molecule was always held perfectly within the simulation box. We used the AMBER parm96 force field[35] for the alanine dipeptide molecule and the TIP3P[36] rigid-body model for the water molecules. The initial values of the alanine-dipeptide dihedral-angles were set to be $\phi = \psi = 180°$ as shown in Fig. 1. We employed a cubic unit cell with periodic boundary conditions. The electrostatic potential was calculated by the Ewald method. We calculated the van der Waals interaction, which is given by the Lennard–Jones 12–6 term, for all pairs of the atoms within the minimum image convention instead of introducing the spherical potential cutoff. The time step was set to $\Delta t = 0.5\,{\rm fs}$.

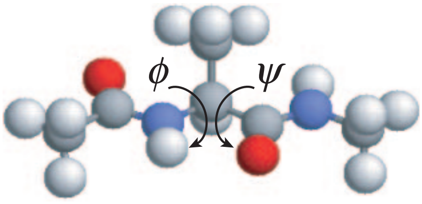

Fig. 1. The initial configuration of alanine dipeptide for the MD simulation. Its dihedral angles are $\phi = \psi = 180°$. The figure was created with RasMol.[37]

In order to obtain an optimal MUBATH weight factor $W_{\rm mbt}(E, V)$, two-dimensional versions[17] of the usual iterative methods[32–34] were used in the preceding MUBATH MD articles.[18,19] In this article, on the other hand, two-dimensional versions of both the iterative methods[32–34] and the energy landscape paving method[38] for multicanonical weight factor determination were employed, because this combination is more efficient to determine $W_{\rm mbt}(E, V)$. The latter is a special case of the Wang–Landau techniques.[39] This technique updates $W_{\rm mbt}(E, V)$ at every MD step n as $W_{\rm mbt}(E, V, n) \equiv \exp[-\{E + P_0V + \delta H(E, V, n)\}/k_{\rm B}T_0]$ to lower energy barriers. First, we updated $\delta H(E, V, n)$ using a histogram of E as in the isobaric–multithermal simulation.[16] Thus, $\delta H(E, V, n)$ is a function of only E and n: $\delta H(E, n)$. The difference $\delta H^{(i)}(E, n)$ between the MUBATH enthalpy and the normal enthalpy at time step n in the i-th iteration is given by[38,39]

$$\delta H^{(i)}(E, n) = \begin{cases} \delta H^{(i-1)}(E) + k_{\rm B}T_0 \log \mathcal{P}^{(i)}(E, n), \\ \qquad\qquad\qquad \text{for } \mathcal{P}^{(i)}(E, n) \geq 1, \\ \delta H^{(i-1)}(E), \quad \text{for } \mathcal{P}^{(i)}(E, n) = 0, \end{cases} \tag{23}$$

where $\mathcal{P}^{(i)}(E, n)$ is the histogram of E accumulated until one time step before n, that is, until time step $(n-1)$. Here, the time step in the i-th iteration takes the values $n = 1, 2, \ldots, N_t^{(i)}$. For the first iteration ($i = 1$), the MUBATH enthalpy starts from the normal enthalpy with

$$\delta H^{(0)}(E) = 0. \tag{24}$$

In the case of $i \geq 2$, $\delta H^{(i-1)}_{\rm mbt}(E)$ is given by the histogram of potential energy $\mathcal{P}^{(i-1)}(E)$ accumulated until the last time step in the $(i-1)$-th iteration as follows:

$$\delta H^{(i-1)}(E) = \begin{cases} \delta H^{(i-2)}(E) + k_{\rm B}T_0\big[\log \mathcal{P}^{(i-1)}(E) - \log \mathcal{P}^{(i-1)}(E_0)\big], \\ \qquad\qquad\qquad \text{for } E \leq E_0 \text{ and } \mathcal{P}^{(i-1)}(E) \geq 1, \\ \delta H^{(i-2)}(E) - k_{\rm B}T_0 \log \mathcal{P}^{(i-1)}(E_0), \\ \qquad\qquad\qquad \text{for } E \leq E_0 \text{ and } \mathcal{P}^{(i-1)}(E) = 0, \\ \delta H^{(i-2)}(E) = 0, \quad \text{for } E > E_0, \end{cases} \tag{25}$$

where $\log \mathcal{P}^{(i-1)}(E)$ was shifted by $\log \mathcal{P}^{(i-1)}(E_0)$ for potential energy less than a threshold E_0 ($E \leq E_0$) to make the potential-energy distribution wider towards the lower value of E. This is because it is easier to widen the potential-energy distribution at high temperature towards the lower values of E than to widen the distribution at low temperature towards the higher values of E. We set the threshold as $E_0 = -400\,\mathrm{kcal\,mol^{-1}} = -1.67 \times 10^3\,\mathrm{kJ\,mol^{-1}}$. We iterated this procedure 18 times ($i = 1$–18) and performed this MD simulation for 10 ps ($N_t^{(1)} = 20000$) in the first iteration. At later iterations, we carried out the MD simulations for longer time, i.e., for 180 ps ($N_t^{(18)} = 360000$) in the 18th iteration. After we elongated $\delta H(E)$ by $\mathcal{P}(E)$, we widen $\delta H(E,V)$ by the histogram $\mathcal{P}(E,V)$ of both E and V as follows:

$$\delta H^{(i)}(E,V,n) = \begin{cases} \delta H^{(i-1)}(E,V) + k_\mathrm{B}T_0 \log \mathcal{P}^{(i)}(E,V,n), \\ \qquad\qquad \text{for } \mathcal{P}^{(i)}(E,V,n) \geq 1, \\ \delta H^{(i-1)}(E,V), \quad \text{for } \mathcal{P}^{(i)}(E,V,n) = 0. \end{cases} \tag{26}$$

We iterated the procedure in Eq. 26 twice, that is, in the 19th and 20th iterations. In the 19th iteration, we used $\delta H^{(i-1)}(E,V)$ calculated from $\log \mathcal{P}^{(i-1)}(E)$ in the 18th iteration shifted by $\log \mathcal{P}^{(i-1)}(E_0)$ in Eq. 25. On the other hand, we did not shift $\log \mathcal{P}^{(i-1)}(E)$ in the 20th iteration and the subsequent MUBATH MD simulation for data collection because $\delta H^{(i-1)}(E,V)$ has been widened both in the E and V space as follows:[32–34]

$$\delta H^{(i-1)}(E,V) = \begin{cases} \delta H^{(i-2)}(E,V) + k_\mathrm{B}T_0 \log \mathcal{P}^{(i-1)}(E,V), \\ \qquad\qquad \text{for } \mathcal{P}^{(i-1)}(E,V) \geq 1, \\ \delta H^{(i-2)}(E,V), \quad \text{for } \mathcal{P}^{(i-1)}(E,V) = 0. \end{cases} \tag{27}$$

We performed the MD simulations for 400 ps in the 19th iteration and for 500 ps in the 20th iteration. An optimal weight factor, $W_\mathrm{mbt}(E,V)$, was obtained after these preliminary simulations for 2.61 ns in total. We then performed a long MUBATH MD simulation for data collection for 10 ns after an equilibration process for 10 ps.

For convenience, we discretized E and V into bins and used histograms to calculate $\delta H(E,V)$. We chose bin sizes of $\Delta E = 20\,\mathrm{kcal\,mol^{-1}} = 84\,\mathrm{kJ\,mol^{-1}}$ and $\Delta V = 0.1\,\mathrm{nm^3}$. In order to calculate the derivative of $\delta H(E,V)$, such as $\partial \delta H(E,V)/\partial E$ and $\partial \delta H(E,V)/\partial V$, it is necessary to interpolate the histogram. We interpolated the histogram by using the third-order polynomial in both E and V to make these derivatives continuous at the boundaries between two adjacent bins (see Ref. 19). Deviation of the value of the Hamiltonian from its initial value is suppressed by this polynomial.

In order to compare the MUBATH simulation with the conventional isobaric–isothermal one, we also performed the isobaric–isothermal MD simulations of the same system, which consists of an alanine dipeptide molecule in 63 water molecules. The initial conditions of these simulations were the same as that for the MUBATH simulation. The simulations were carried out for 1 ns each at $(T_0, P_0) = (240\,\mathrm{K}, 0.1\,\mathrm{MPa})$, (298 K, 0.1 MPa), and (298 K, 300 MPa).

Results and Discussion

Figures 2a, 2b, and 2c show the time series of potential energy E in the isobaric–isothermal MD simulation at $(T_0, P_0) =$ (240 K, 0.1 MPa), (298 K, 0.1 MPa), and (298 K, 300 MPa), respectively. The potential energy fluctuated in a narrow range. The fluctuation ranges were $E = -730$–$-640\,\mathrm{kcal\,mol^{-1}} = -3.0$–$-2.7 \times 10^3\,\mathrm{kJ\,mol^{-1}}$ at $(T_0, P_0) = (240\,\mathrm{K}, 0.1\,\mathrm{MPa})$, $E = -680$–$-570\,\mathrm{kcal\,mol^{-1}} = -2.8$–$-2.4 \times 10^3\,\mathrm{kJ\,mol^{-1}}$ at $(T_0, P_0) = (298\,\mathrm{K}, 0.1\,\mathrm{MPa})$, and $E = -690$–$-590\,\mathrm{kcal\,mol^{-1}} = -2.9$–$-2.5 \times 10^3\,\mathrm{kJ\,mol^{-1}}$ at $(T_0, P_0) = (298\,\mathrm{K}, 300\,\mathrm{MPa})$. On the other hand, Figure 2d shows that the MUBATH MD simulation realized a random walk in the potential-energy space and covered a wide energy range. The covered range was $E = -730$–$-280\,\mathrm{kcal\,mol^{-1}} = -3.1$–$-1.2 \times 10^3\,\mathrm{kJ\,mol^{-1}}$ and 4–5 times wider than that by the isobaric–isothermal MD simulations.

Figures 3a–3c show the time series of volume V obtained by the conventional isobaric–isothermal MD simulations. The volume fluctuation ranges were $V = 1.9$–$2.4\,\mathrm{nm^3}$ at $(T_0, P_0) = (240\,\mathrm{K}, 0.1\,\mathrm{MPa})$, 1.9–2.5 nm^3 at $(T_0, P_0) = (298\,\mathrm{K}, 0.1\,\mathrm{MPa})$, and 1.8–2.1 nm^3 at $(T_0, P_0) = (298\,\mathrm{K}, 300\,\mathrm{MPa})$. The MUBATH MD simulation, on the other hand, performed a random walk that covers a range of $V = 1.8$–$3.5\,\mathrm{nm^3}$, as shown in Fig. 3d, which is 3–5 times wider than that by the isobaric–isothermal MD simulations. Such a large fluctuation of V can be realized by the MUBATH algorithm. It is not possible by the multicanonical algorithm. The multicanonical algorithm can realize a random walk only in the potential energy space; however, there is no fluctuation in the volume space.

Figure 4 shows the time series of the dihedral angle ϕ. The dihedral angle ϕ rotated about half a turn (covering a 180° range) in the isobaric–isothermal MD simulations. This fact shows that it is trapped in local-minimum free-energy states and does not rotate beyond the energy barriers. In the MUBATH MD simulation, on the other hand, ϕ underwent a complete rotation (covering 360°) three times (three turns) in the time range of 1 ns as shown in Fig. 4d. It made 24 turns throughout the simulation of 10 ns. Here, we define one turn of rotation when ϕ undergoes all values between -180 and 180° and count another turn when ϕ undergoes all the values after that.

We show the time series of the dihedral angle ψ in Fig. 5. Similar to the case of ϕ, the isobaric–isothermal MD simulation tended to be trapped in local-minimum free-energy states. The dihedral angle ψ did not make entire rotation during 1 ns at $(T_0, P_0) = (240\,\mathrm{K}, 0.1\,\mathrm{MPa})$, as shown in Fig. 5a. As the temperature was increased, ψ began to undergo complete rotation. ψ makes one turn at $(T_0, P_0) = (298\,\mathrm{K}, 0.1\,\mathrm{MPa})$ and two turns at $(T_0, P_0) = (298\,\mathrm{K}, 300\,\mathrm{MPa})$, as shown in Fig. 5b and Fig. 5c, respectively. The efficiency of the MUBATH MD for ψ is more remarkable than that for ϕ. The dihedral angle ψ underwent 24 complete rotations in 1 ns, as shown in Fig. 5d. It made 242 turns during the 10 ns simulation. The wide rotation ranges of ϕ and ψ show that the simulation in the MUBATH ensemble can escape from local-minimum free-energy states and samples the configurational space much more widely than the conventional isobaric–isothermal ensemble.

There are two reasons of the high sampling efficiency for dihedral angles in the MUBATH simulation. One reason is that the sampling in a wide range of potential energy makes the simulation overcome the potential energy barrier between the states in the dihedral angle space. The other is that when V is large, the number density of water molecules around the peptide is less than that when V is small. This means a decrease in the obstacles (water molecules) and makes the

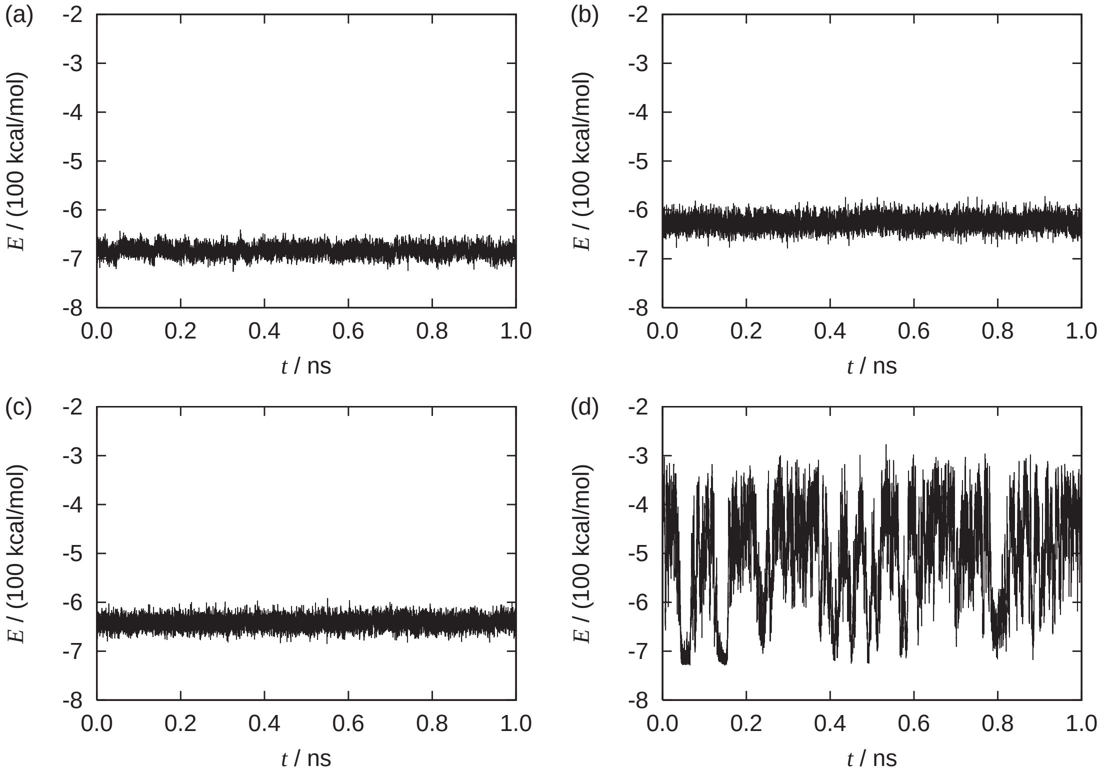

Fig. 2. The time series of potential energy E from (a) the conventional isobaric–isothermal MD simulation at $T_0 = 240\,\mathrm{K}$ and $P_0 = 0.1\,\mathrm{MPa}$, (b) the conventional isobaric–isothermal MD simulation at $T_0 = 298\,\mathrm{K}$ and $P_0 = 0.1\,\mathrm{MPa}$, (c) the conventional isobaric–isothermal MD simulation at $T_0 = 298\,\mathrm{K}$ and $P_0 = 300\,\mathrm{MPa}$, and (d) the multibaric–multithermal MD simulation.

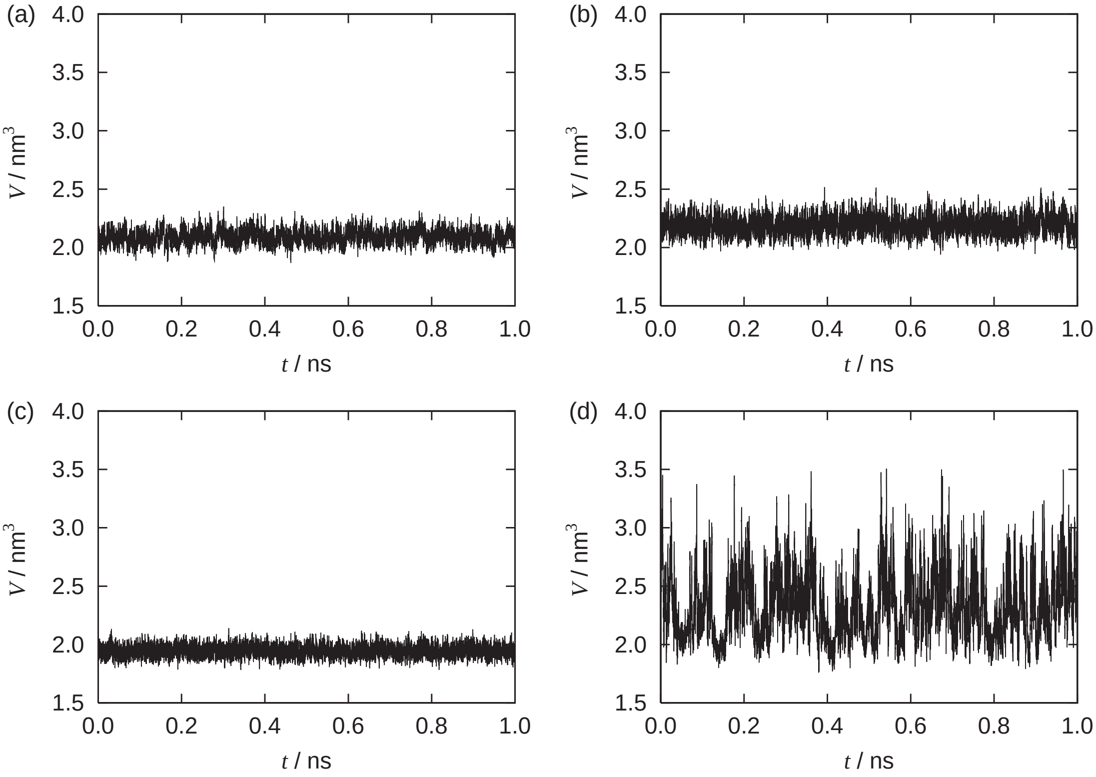

Fig. 3. The time series of volume V from (a) the conventional isobaric–isothermal MD simulation at $T_0 = 240\,\mathrm{K}$ and $P_0 = 0.1$ MPa, (b) the conventional isobaric–isothermal MD simulation at $T_0 = 298\,\mathrm{K}$ and $P_0 = 0.1\,\mathrm{MPa}$, (c) the conventional isobaric–isothermal MD simulation at $T_0 = 298\,\mathrm{K}$ and $P_0 = 300\,\mathrm{MPa}$, and (d) the multibaric–multithermal MD simulation.

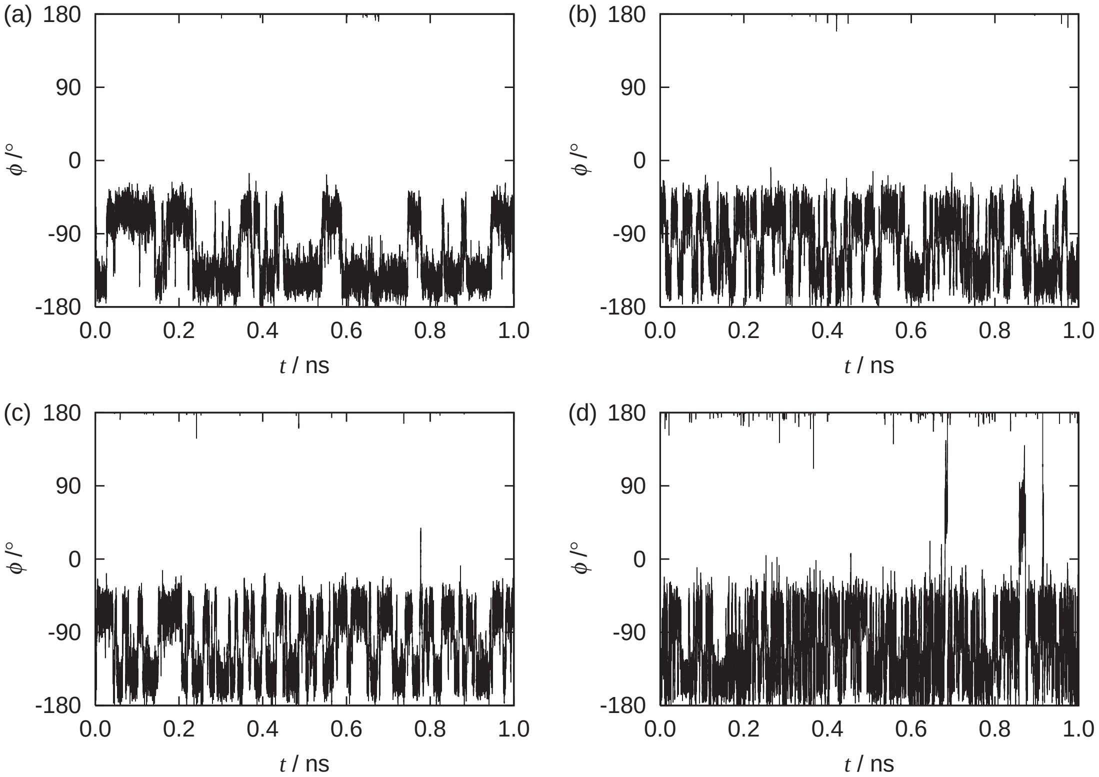

Fig. 4. The time series of the backbone dihedral angle ϕ from (a) the conventional isobaric–isothermal MD simulation at $T_0 = 240$ K and $P_0 = 0.1$ MPa, (b) the conventional isobaric–isothermal MD simulation at $T_0 = 298$ K and $P_0 = 0.1$ MPa, (c) the conventional isobaric–isothermal MD simulation at $T_0 = 298$ K and $P_0 = 300$ MPa, and (d) the multibaric–multithermal MD simulation.

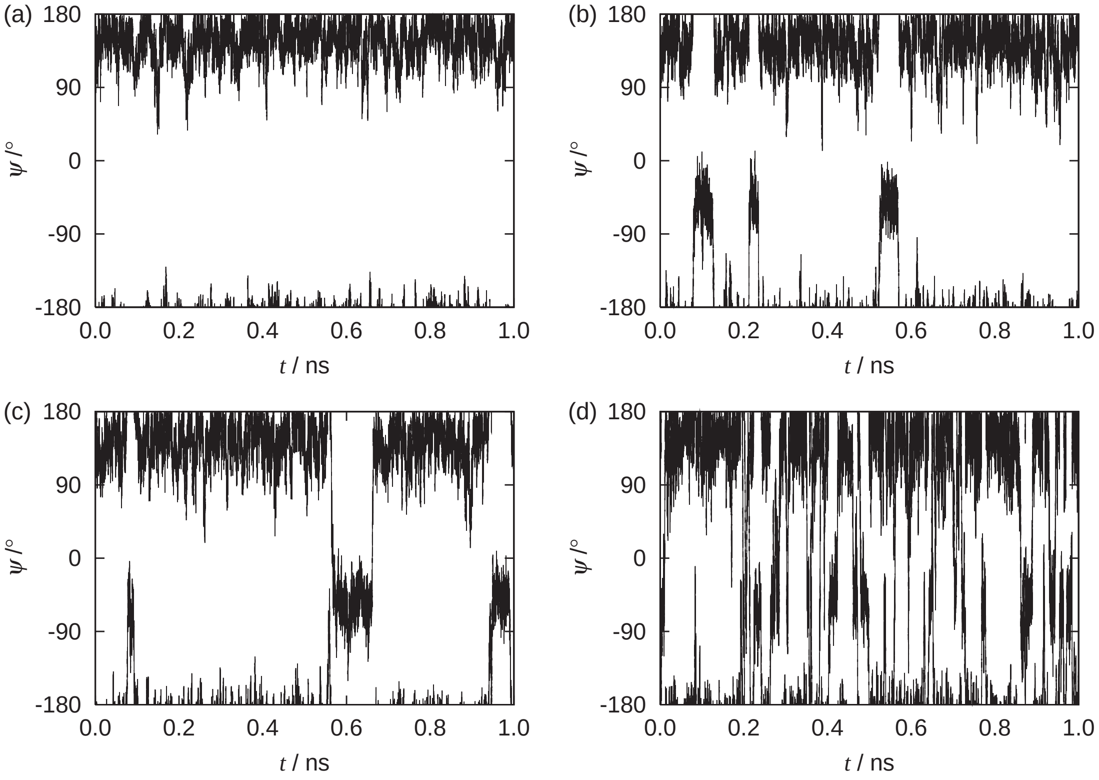

Fig. 5. The time series of the backbone dihedral angle ψ from (a) the conventional isobaric–isothermal MD simulation at $T_0 = 240$ K and $P_0 = 0.1$ MPa, (b) the conventional isobaric–isothermal MD simulation at $T_0 = 298$ K and $P_0 = 0.1$ MPa, (c) the conventional isobaric–isothermal MD simulation at $T_0 = 298$ K and $P_0 = 300$ MPa, and (d) the multibaric–multithermal MD simulation.

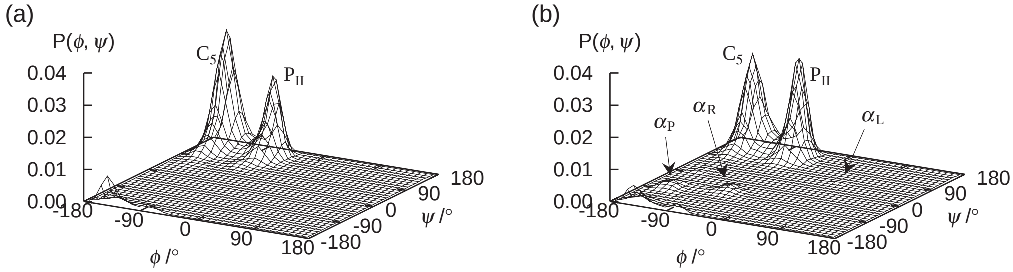

Fig. 6. The probability distributions $\mathscr{P}(\phi, \psi)$ of the backbone dihedral angles ϕ and ψ at $T = 240\,\mathrm{K}$ and $P = 0.1\,\mathrm{MPa}$, which were obtained (a) from the conventional isobaric–isothermal MD simulation and (b) by the reweighting techniques from the results of the multibaric–multithermal MD simulation.

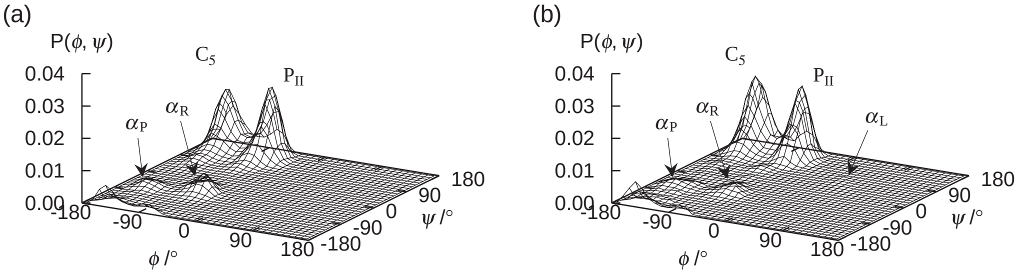

Fig. 7. The probability distributions $\mathscr{P}(\phi, \psi)$ of the backbone dihedral angles ϕ and ψ at $T = 298\,\mathrm{K}$ and $P = 0.1\,\mathrm{MPa}$, which were obtained (a) from the conventional isobaric–isothermal MD simulation and (b) by the reweighting techniques from the results of the multibaric–multithermal MD simulation.

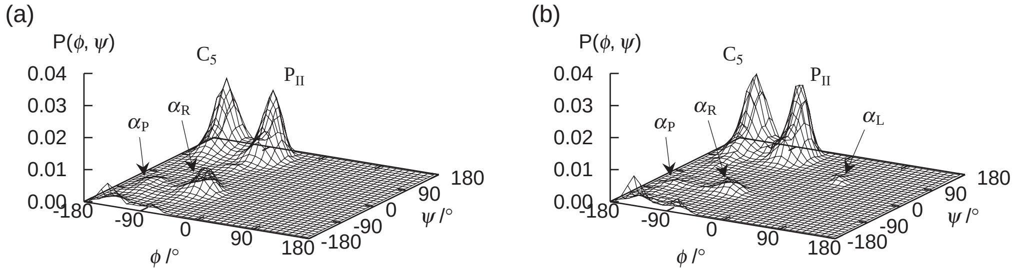

Fig. 8. The probability distributions $\mathscr{P}(\phi, \psi)$ of the backbone dihedral angles ϕ and ψ at $T = 298\,\mathrm{K}$ and $P = 300\,\mathrm{MPa}$, which were obtained (a) from the conventional isobaric–isothermal MD simulation and (b) by the reweighting techniques from the results of the multibaric–multithermal MD simulation.

rotation of ϕ and ψ easier. Although the multicanonical algorithm has high sampling efficiency due to the former effect, the latter arises from the MUBATH algorithm.

The probability distributions $\mathscr{P}(\phi, \psi)$ of ϕ and ψ at $T = 240\,\mathrm{K}$ and $P = 0.1\,\mathrm{MPa}$ are shown in Fig. 6. We discretized ϕ and ψ using the bin sizes of $\Delta\phi = \Delta\psi = 10^\circ$ to calculate $\mathscr{P}(\phi, \psi)$ as a histogram. Figure 6a shows that $\mathscr{P}(\phi, \psi)$ obtained by the isobaric–isothermal MD simulation has only two peaks: $\mathrm{P_{II}}$ and $\mathrm{C_5}$. No other state was sampled by the isobaric–isothermal MD simulation. It means that the isobaric–isothermal MD was trapped in the local minima of $\mathrm{P_{II}}$ and $\mathrm{C_5}$. Figure 6b shows $\mathscr{P}(\phi, \psi)$ obtained by the reweighting procedure of Eq. 22 at $T = 240\,\mathrm{K}$ and $P = 0.1\,\mathrm{MPa}$ from the MUBATH MD simulation. The MUBATH MD simulation sampled not only the states of $\mathrm{P_{II}}$ and $\mathrm{C_5}$ but also the states of α_R, α_P, and α_L. These results indicate again that the MUBATH simulation can get over the free-energy barriers and has a high sampling efficiency.

The probability distribution $\mathscr{P}(\phi, \psi)$ at $(T, P) = (298\,\mathrm{K}, 0.1\,\mathrm{MPa})$ and $(298\,\mathrm{K}, 300\,\mathrm{MPa})$ are shown in Fig. 7 and Fig. 8, respectively. Although the isobaric–isothermal MD simulations sampled the four states of $\mathrm{P_{II}}$, $\mathrm{C_5}$, α_R, and α_P, it could not sample the α_L state both at $(T, P) = (298\,\mathrm{K}, 0.1\,\mathrm{MPa})$ and $(298\,\mathrm{K}, 300\,\mathrm{MPa})$, as shown in Fig. 7a and Fig. 8a, respectively. On the other hand, the MUBATH simulation did sample the α_L state as well as the $\mathrm{P_{II}}$, $\mathrm{C_5}$, α_R, and α_P states, as shown in Fig. 7b and Fig. 8b. The peak position of $\mathscr{P}(\phi, \psi)$ for each state at $T = 298\,\mathrm{K}$ and $P = 0.1\,\mathrm{MPa}$ is shown in Table 1.

The volume under the surface $\mathscr{P}(\phi, \psi)$ around each peak corresponds to the population W of each state. In order to calculate W, the whole (ϕ, ψ) plane was divided into six states as shown in Fig. 9 and Table 2. For example, the population $W_{\mathrm{P_{II}}}$ of the P_{II} state is calculated by the integral of $\mathscr{P}(\phi, \psi)$ in the area in which ϕ and ψ take the $\mathrm{P_{II}}$ configuration:

$$W_{\mathrm{P_{II}}} = \int_{(\phi,\psi)\in \mathrm{P_{II}}} \mathrm{d}\phi\, \mathrm{d}\psi\ \mathscr{P}(\phi, \psi), \tag{28}$$

where the integration range of (ϕ, ψ) stands for the range for the corresponding state in Table 2. The population of each state at $T = 298\,\mathrm{K}$ and $P = 0.1\,\mathrm{MPa}$ is also shown in Table 2. The statistical uncertainties were estimated by using the jackknife method[40] in which the production run is divided into ten segments. Figure 9 shows clear peaks for the $\mathrm{P_{II}}$, $\mathrm{C_5}$, α_R, α_P, and α_L states. Although no clear peak has been observed for the $\mathrm{C_7^{ax}}$ state in Fig. 7b, Figure 9 shows some finite probability in the logarithmic scale for the $\mathrm{C_7^{ax}}$ state as well.

Table 1. Peak Positions (ϕ, ψ) of the Probability Distribution $\mathcal{P}(\phi, \psi)$ for Five States at $T = 298\,\mathrm{K}$ and $P = 0.1\,\mathrm{MPa}$[a)]

State[b)]	ϕ	ψ
$\mathrm{P_{II}}$	−65°	145°
$\mathrm{C_5}$	−145°	155°
α_R	−65°	−45°
α_P	−145°	−65°
α_L	35°	85°

a) The results were obtained by the reweighting techniques from the MUBATH MD simulation. b) Taken from Ref. 25.

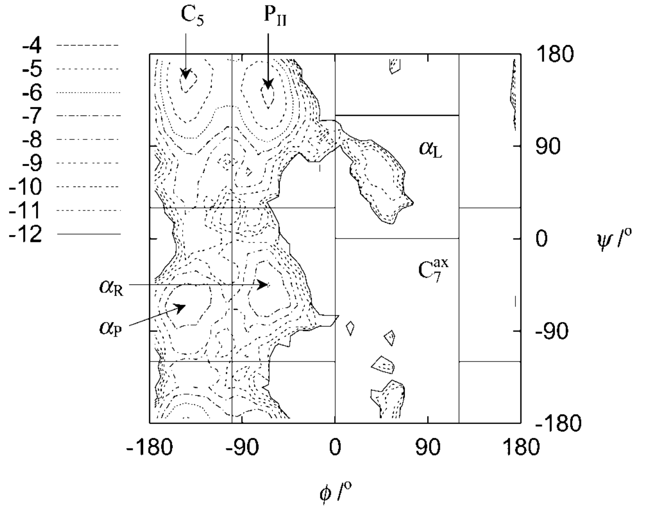

Fig. 9. Contour map for $\log \mathcal{P}(\phi, \psi)$ at $T = 298\,\mathrm{K}$ and $P = 300\,\mathrm{MPa}$, which was obtained by the reweighting techniques from the results of the multibaric–multithermal MD simulation. The whole (ϕ, ψ) plane is divided into six states of $\mathrm{C_5}$, $\mathrm{P_{II}}$, α_P, α_R, α_L, and $\mathrm{C_7^{ax}}$ by the solid horizontal and vertical lines.

Estimation of the partial molar enthalpy and partial molar volume is important in solution chemistry because these values control the population of each state when temperature and pressure are changed. There is, to our knowledge, no MD study to calculate the partial molar enthalpy and partial molar volume in a biomolecular system, because the sampling efficiency of the conventional isobaric–isothermal algorithm is low and the multicanonical algorithm cannot specify pressure or change volume. The MUBATH algorithm makes it possible to calculate the partial molar enthalpy and partial molar volume.

Figure 10 shows the population ratios of $W_{\mathrm{C_5}}/W_{\mathrm{P_{II}}}$, $W_{\alpha_\mathrm{R}}/W_{\mathrm{P_{II}}}$, $W_{\alpha_\mathrm{P}}/W_{\mathrm{P_{II}}}$, and $W_{\alpha_\mathrm{L}}/W_{\mathrm{P_{II}}}$ as functions of the inverse of temperature $1/T$ at the constant pressure of $P = 0.1\,\mathrm{MPa}$. As the temperature increased, $W_{\mathrm{C_5}}/W_{\mathrm{P_{II}}}$, $W_{\alpha_\mathrm{R}}/W_{\mathrm{P_{II}}}$, and $W_{\alpha_\mathrm{P}}/W_{\mathrm{P_{II}}}$ increased, although the error in $W_{\alpha_\mathrm{L}}/W_{\mathrm{P_{II}}}$ was too large to discuss its temperature dependence. From thermodynamics, the increase in temperature at a constant pressure causes the increase of enthalpy. The increases in the population ratios $W/W_{\mathrm{P_{II}}}$ against the $\mathrm{P_{II}}$ state by the temperature increase indicate that enthalpy for the $\mathrm{C_5}$, α_R, and α_P states is higher than that of the $\mathrm{P_{II}}$ state. The difference in partial molar enthalpy (ΔH) of the $\mathrm{C_5}$ state from that of the $\mathrm{P_{II}}$ state is calculated from the derivative of $W_{\mathrm{C_5}}/W_{\mathrm{P_{II}}}$ with respect to $1/T$:

$$\Delta H = -R\left[\frac{\partial(W_{\mathrm{C_5}}/W_{\mathrm{P_{II}}})}{\partial(1/T)}\right]_P, \tag{29}$$

where R is the gas constant: $R = 8.3145\,\mathrm{J\,mol^{-1}\,K^{-1}}$. The

Table 2. Dihedral Angle Ranges of (ϕ, ψ) for Six States and Their Population at $T = 298\,\mathrm{K}$ and $P = 0.1\,\mathrm{MPa}$

State	ϕ	ψ	Population[a)]
$\mathrm{P_{II}}$	(−100°, 0°)	(30°, −120°)	0.412(18)[b)]
$\mathrm{C_5}$	(120°, −100°)	(30°, −120°)	0.496(20)
α_R	(−100°, 0°)	(−120°, 30°)	0.041(6)
α_P	(120°, −100°)	(−120°, 30°)	0.046(10)
α_L	(0°, 120°)	(0°, 120°)	0.004(4)
$\mathrm{C_7^{ax}}$	(0°, 120°)	(120°, 0°)	0.0008(7)

a) The results were obtained by the reweighting techniques from the MUBATH MD simulation. b) The numbers in parentheses for the population are the estimated uncertainties.

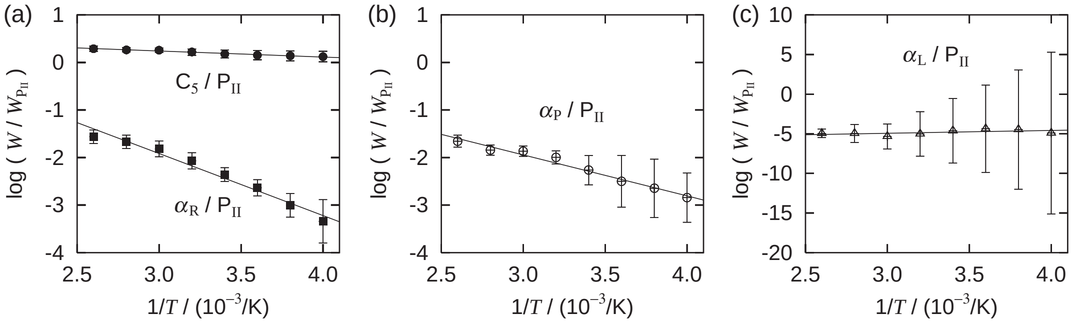

Fig. 10. The population ratios as functions of the inverse of temperature $1/T$ at constant pressure of $P = 0.1\,\mathrm{MPa}$, which was obtained by the reweighting techniques from the results of the multibaric–multithermal MD simulation: (a) those of $W_{\mathrm{C_5}}/W_{\mathrm{P_{II}}}$ and $W_{\alpha_\mathrm{R}}/W_{\mathrm{P_{II}}}$, (b) that of $W_{\alpha_\mathrm{P}}/W_{\mathrm{P_{II}}}$, and (c) that of $W_{\alpha_\mathrm{L}}/W_{\mathrm{P_{II}}}$.

Table 3. Differences in Partial Molar Enthalpy ΔH/ kJ mol^{-1} of the C_5, α_R, α_P, and α_L States from That of the P_{II} State

State	MUBATH MD	Raman[a)]
C_5	1.1 ± 0.9	2.5
α_R	10.8 ± 2.8	4.4
α_P	7.2 ± 4.3	—
α_L	-3 ± 56	—

a) Taken from Ref. 26.

Table 4. Differences in Partial Molar Volume ΔV/ cm^3 mol^{-1} of the C_5, α_R, α_P, and α_L States from That of the P_{II} State

State	MUBATH MD	Raman[a)]	RISM–KB[a)]
C_5	0.7 ± 0.9	0.1	-1.8
α_R	-1.2 ± 5.4	1.1	-1.2
α_P	2.8 ± 2.6	—	—
α_L	-8 ± 12	—	—

a) Taken from Ref. 26.

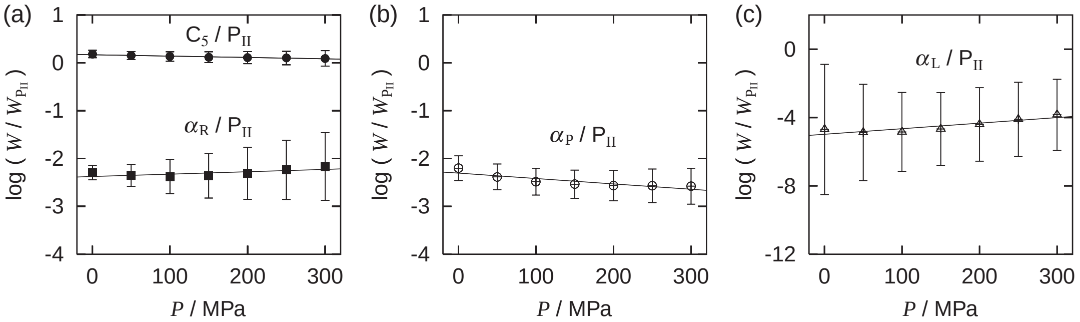

Fig. 11. The population ratios as functions of pressure P at constant temperature of $T = 298$ K, which was obtained by the reweighting techniques from the results of the multibaric–multithermal MD simulation: (a) those of $W_{C_5}/W_{P_{II}}$ and $W_{\alpha_R}/W_{P_{II}}$, (b) that of $W_{\alpha_P}/W_{P_{II}}$, and (c) that of $W_{\alpha_L}/W_{P_{II}}$.

derivative of $W_{C_5}/W_{P_{II}}$ was calculated here by the least-squares fitting. The error bars were estimated by the jackknife method[40] in which the production run was divided into ten segments again. The differences between the partial molar enthalpy of the α_R, α_P, and α_L states and that of the P_{II} state were also obtained in the same way. The ΔH values are shown in Table 3.

Table 3 also shows that the experimental data by Raman spectroscopy for the C_5 and α_R states.[26] The α_P and α_L states were not observed by the Raman spectroscopy experiment. According to the authors of Ref. 26, the Raman spectroscopy results should have error bars larger than those given in Ref. 26, because there are other experimental errors that have not been taken into account.[41] Considering these errors, ΔH obtained from the MUBATH MD simulation agree well with those from the Raman spectroscopy.

The RISM theory[42–44] can be used to calculate thermodynamical quantities in aqueous solution. Takekiyo et al. have tried to compare the Raman spectroscopy data with those obtained from RISM theory.[26] In this case, however, the authors do not report ΔH because of significant uncertainties in enthalpy.[26]

The multicanonical method is another simulation technique to escape from local-minimum free-energy states. It is also popular for biomolecular simulations. Although it can change temperature, it does not fix pressure, but volume. Accordingly, with the multicanonical algorithm, we cannot study the temperature dependence of the peptide structures under the same pressure as well as under the experimental conditions and we cannot calculate ΔH.

The conventional isobaric–isothermal MD simulation can specify both temperature and pressure. However, it gets trapped in local-minimum free-energy states as shown in Fig. 6. For this reason, the sampling efficiency is low for biomolecules.

The MUBATH method has the merits of both multicanonical algorithm and isobaric–isothermal method. It can escape from local-minimum free-energy states and specify temperature and pressure. The MUBATH method, therefore, enables us to calculate accurate ΔH among several states of a peptide. As far as we know, this is the first computational work to calculate ΔH of a peptide.

Figure 11 shows the population ratios of $W_{C_5}/W_{P_{II}}$, $W_{\alpha_R}/W_{P_{II}}$, $W_{\alpha_P}/W_{P_{II}}$, and $W_{\alpha_L}/W_{P_{II}}$ as functions of P at the constant temperature of $T = 298$ K. As the pressure increased, both $W_{C_5}/W_{P_{II}}$ and $W_{\alpha_P}/W_{P_{II}}$ decreased, although the error in $W_{\alpha_R}/W_{P_{II}}$ and $W_{\alpha_L}/W_{P_{II}}$ was too large to discuss the pressure dependence. An increase in pressure at constant temperature generally causes a decrease in the volume. The decreases in $W_{C_5}/W_{P_{II}}$ and $W_{\alpha_P}/W_{P_{II}}$ means that V values of the C_5 and α_P states are larger than that of P_{II}. The difference in partial molar volume (ΔV) of the C_5 state from that of the P_{II} state are calculated from the derivative of $W_{C_5}/W_{P_{II}}$ with respect to P by

$$\Delta V = -RT\left[\frac{\partial(W_{C_5}/W_{P_{II}})}{\partial P}\right]_T. \tag{30}$$

The difference between the partial molar volume of the α_R, α_P, and α_L states and that of the P_{II} state was also obtained in the same way. The values of ΔV are shown in Table 4. The value of ΔV between C_5 and P_{II} and that between α_R and P_{II} obtained by the MUBATH MD simulation agree well with those from Raman spectroscopy. The partial molar volume difference ΔV that was calculated by the RISM–Kirkwood–Buff (KB) theory is also shown in Table 4.[26] The difference ΔV between C_5 and P_{II} was lower by the RISM–KB theory than by the MUBATH MD simulation and by the Raman spectroscopy. On the other hand, ΔV between α_R and P_{II} agrees with the MUBATH MD simulation within its error bar.

As discussed above, the multicanonical simulation can escape from local-minimum free-energy states, but cannot change volume. The conventional isobaric–isothermal MD simulation can change volume, but is trapped in a local free energy minimum. Therefore, the partial molar volume cannot be calculated by these simulation methods. The MUBATH method has the merits of both methods and is a very effective simulation technique to calculate ΔV.

Conclusion

We applied the MUBATH MD method to alanine dipeptide in explicit water. This method has an advantage that the simulation performs a two-dimensional random walk both in the potential-energy space and in the volume space so that it allows the simulation to escape from local-minimum free-energy states. It sampled the states of $\mathrm{P_{II}}$, $\mathrm{C_5}$, α_R, α_P, and α_L. On the other hand, the conventional isobaric–isothermal simulation was trapped in local-minimum free-energy states and sampled not all of them.

Other advantages of the MUBATH MD method are that one can control temperature and pressure as in real experimental conditions and that one can obtain various isobaric–isothermal ensemble averages from only one simulation run. We calculated the temperature and pressure dependences of the population for the states of $\mathrm{P_{II}}$, $\mathrm{C_5}$, α_R, α_P, and α_L. From these temperature and pressure dependences, the differences in the partial molar enthalpy ΔH and the partial molar volume ΔV were calculated between the $\mathrm{P_{II}}$ state and other states. The values of ΔH and ΔV were in accord with the Raman spectroscopy data. The MUBATH method is therefore a powerful simulation technique to calculate ΔH and ΔV. It overcomes the difficulty of the multicanonical method, in which a volume change is not allowed, and that of the isobaric–isothermal method, in which the simulation gets trapped in states of local free-energy minima.

In order to study the temperature and pressure dependences of the protein structures, one has to investigate its free energy surface at several values of temperature and pressure. The MUBATH method will thus be of great use for the protein folding problem under various conditions of temperature and pressure.

This work was supported, in part, by the Grants-in-Aid for the Next Generation Super Computing Project, Nanoscience Program and for Scientific Research in Priority Areas, "Water and Biomolecules," from the Ministry of Education, Culture, Sports, Science and Technology, Japan.

References

1 S. Nosé, *Mol. Phys.* **1984**, *52*, 255.

2 S. Nosé, *J. Chem. Phys.* **1984**, *81*, 511.

3 W. G. Hoover, *Phys. Rev. A* **1985**, *31*, 1695.

4 N. Metropolis, A. W. Rosenbluth, M. N. Rosenbluth, A. H. Teller, E. Teller, *J. Chem. Phys.* **1953**, *21*, 1087.

5 H. C. Andersen, *J. Chem. Phys.* **1980**, *72*, 2384.

6 I. R. McDonald, *Mol. Phys.* **1972**, *23*, 41.

7 U. H. E. Hansmann, Y. Okamoto, in *Annual Reviews of Computational Physics VI*, ed. by D. Stauffer, World Scientific, Singapore, **1999**, p. 129.

8 A. Mitsutake, Y. Sugita, Y. Okamoto, *Biopolymers (Pept. Sci.)* **2001**, *60*, 96.

9 B. A. Berg, *Comput. Phys. Commun.* **2002**, *104*, 52.

10 B. A. Berg, T. Neuhaus, *Phys. Lett. B* **1991**, *267*, 249.

11 B. A. Berg, T. Neuhaus, *Phys. Rev. Lett.* **1992**, *68*, 9.

12 U. H. E. Hansmann, Y. Okamoto, F. Eisenmenger, *Chem. Phys. Lett.* **1996**, *259*, 321.

13 N. Nakajima, H. Nakamura, A. Kidera, *J. Phys. Chem. B* **1997**, *101*, 817.

14 A. M. Ferrenberg, R. H. Swendsen, *Phys. Rev. Lett.* **1988**, *61*, 2635; **1989**, *63*, 1658.

15 H. Okumura, Y. Okamoto, *Chem. Phys. Lett.* **2004**, *383*, 391.

16 H. Okumura, Y. Okamoto, *Phys. Rev. E* **2004**, *70*, 026702.

17 H. Okumura, Y. Okamoto, *J. Phys. Soc. Jpn.* **2004**, *73*, 3304.

18 H. Okumura, Y. Okamoto, *Chem. Phys. Lett.* **2004**, *391*, 248.

19 H. Okumura, Y. Okamoto, *J. Comput. Chem.* **2006**, *27*, 379.

20 I. R. Gould, P. A. Kollman, *J. Phys. Chem.* **1992**, *96*, 9255.

21 J. Apostolakis, P. Ferrara, A. Caflisch, *J. Chem. Phys.* **1999**, *110*, 2099.

22 P. E. Smith, *J. Chem. Phys.* **1999**, *111*, 5568.

23 A. D. Mackerell, Jr., M. Feig, C. L. Brooks, III, *J. Comput. Chem.* **2004**, *25*, 1400.

24 D. S. Chekmarev, T. Ishida, R. M. Levy, *J. Phys. Chem. B* **2004**, *108*, 19487.

25 J. D. Chodera, W. C. Swope, J. W. Pitera, K. A. Dill, *Multiscale Modell. Simul.* **2006**, *5*, 1214.

26 T. Takekiyo, T. Imai, M. Kato, Y. Taniguchi, *Biopolymers* **2004**, *73*, 283.

27 H. Okumura, S. G. Itoh, Y. Okamoto, *J. Chem. Phys.* **2007**, *126*, 084103.

28 T. F. Miller, M. Eleftheriou, P. Pattnaik, A. Ndirango, D. Newns, G. J. Martyna, *J. Chem. Phys.* **2002**, *116*, 8649.

29 H. Yoshida, *Phys. Lett. A* **1990**, *150*, 262.

30 S. D. Bond, B. J. Leimkuhler, B. B. Laird, *J. Comput. Phys.* **1999**, *151*, 114.

31 S. Nosé, *J. Phys. Soc. Jpn.* **2001**, *70*, 75.

32 B. A. Berg, T. Celik, *Phys. Rev. Lett.* **1992**, *69*, 2292.

33 J. Lee, *Phys. Rev. Lett.* **1993**, *71*, 211; **1993**, *71*, 2353.

34 Y. Okamoto, U. H. E. Hansmann, *J. Phys. Chem.* **1995**, *99*, 11276.

35 P. A. Kollman, R. Dixon, W. Cornell, T. Fox, C. Chipot, A. Pohorille, in *Computer Simulation of Biomolecular Systems 3*, ed. by A. Wilkinson, P. Weiner, W. F. van Gunsteren, Elsevier, Dordrecht, **1997**, p. 83.

36 W. L. Jorgensen, J. Chandrasekhar, J. D. Madura, R. W. Impey, M. L. Klein, *J. Chem. Phys.* **1983**, *79*, 926.

37 R. A. Sayle, E. J. Milner-White, *Trends Biochem. Sci.* **1995**, *20*, 374.

38 U. H. E. Hansmann, L. T. Wille, *Phys. Rev. Lett.* **2002**, *88*, 068105.

39 F. Wang, D. P. Landau, *Phys. Rev. Lett.* **2001**, *86*, 2050.

40 B. A. Berg, *Introduction to Monte Carlo Simulations and Their Statistical Analysis*, World Scientific, Singapore, **2004**.

41 T. Takekiyo, T. Imai, M. Kato, private communications.

42 D. Chandler, *J. Chem. Phys.* **1977**, *67*, 1113.

43 F. Hirata, P. J. Rossky, *Chem. Phys. Lett.* **1981**, *83*, 329.

44 J. S. Perkyns, B. M. Pettitt, *Chem. Phys. Lett.* **1992**, *190*, 626.